Int J Appl Earth Obs Geoinformation 69 (2018) 56–63

Contents lists available at ScienceDirect

Int J Appl Earth Obs Geoinformation

journal homepage: www.elsevier.com/locate/jag

Global linkages between teleconnection patterns and the terrestrial biosphere

Kyla M. Dahlin[a,*], Toby R. Ault[b]

[a] Michigan State University, Department of Geography, Environment, & Spatial Sciences and Program in Ecology, Evolutionary Biology, & Behavior, United States
[b] Cornell University, Department of Earth and Atmospheric Sciences, United States

ARTICLE INFO

Keywords:
Biosphere-atmosphere interactions
Teleconnections
Leaf area index
Global ecology

ABSTRACT

Interannual variability in the global carbon cycle is largely due to variations in carbon uptake by terrestrial ecosystems, yet linkages between climate variability and variability in the terrestrial carbon cycle are not well understood at the global scale. Using a 30-year satellite record of semi-monthly leaf area index (LAI), we show that four modes of climate variability – El Niño/Southern Oscillation, the North Atlantic Oscillation, the Atlantic Meridional Mode, and the Indian Ocean Dipole Mode – strongly impact interannual vegetation growth patterns, with 68% of the land surface impacted by at least one of these teleconnection patterns, yet the spatial distribution of these impacts is heterogeneous. Considering the patterns' impacts by biome, none has an exclusively positive or negative relationship with LAI. Our findings imply that future changes in the frequency and/or magnitude of teleconnection patterns will lead to diverse changes to the terrestrial biosphere and the global carbon cycle.

1. Introduction

Climate fluctuations affect the terrestrial biosphere across seasonal to multi-decadal timescales (Stenseth et al., 2003), while vegetation on the land surface helps regulate the flow of energy, carbon, and water through the climate system. This biosphere-atmosphere coupling will influence the rate of increases in greenhouse gas concentration in the atmosphere, the pace of climate change, the magnitude and scope of biodiversity loss, and the interconnection between food, water, and energy that is the basis of food security this century (Bonan, 2008; Ogutu and Owen-Smith, 2003). However, the sign and magnitude of atmospheric effects on land surface vegetation remains poorly constrained, partly because biosphere-atmosphere coupling depends strongly on season, biome, and timescale, and biosphere-atmosphere feedbacks can have downstream effects on ecological communities (e.g. Charrette et al., 2006; Maza-Villalobos et al., 2013; Ogutu and Owen-Smith, 2003). Further uncertainty arises from a mismatch of spatial and temporal scales at which meteorological and ecological data are collected. Climate datasets typically span several decades with near global coverage at 10–100 km spatial resolution (Phillips et al., 2014), while long-term ecological monitoring studies often focus on finer spatial grain sizes and smaller spatial extents. Remotely sensed data can be used to bridge these scale gaps because they span more than three decades (AVHRR/MODIS/VIIRS, LandSat), and they are produced at spatial resolutions that fall between meteorological and in-situ ecological monitoring scales. Such products permit us to analyze how variations driven by large-scale climate phenomena affect global vegetation activity via large scale climate fluctuation patterns like hemispheric and global teleconnections.

Teleconnections patterns are persistent atmospheric circulation patterns that span large distances. They are defined statistically (Barnston and Livezey, 1987) and can be used to characterize changes in local and regional "packages of weather" (Stenseth et al., 2003) associated with different states of climate modes. Two well known teleconnection patterns are El Niño-Southern Oscillation (ENSO) and the North Atlantic Oscillation (NAO). Connecting vegetation responses to teleconnections patterns is challenging because ecosystems may react to different meteorological variables, like temperature or precipitation, across multiple time lags (McPhaden et al., 2006). For example, a positive wintertime NAO is correlated with earlier, higher than average springtime vegetation growth in Europe (Li et al., 2016). Despite these obstacles, weather events associated with ENSO and the NAO have been tied to changes in ungulate populations in South Africa (Ogutu and Owen-Smith, 2003), butterflies in Borneo (Charrette et al., 2006), forest succession in Mexico (Maza-Villalobos et al., 2013), and more (Stenseth et al., 2003). While many of the studies focused on connections between teleconnection patterns and the biosphere have focused on ENSO, recently some studies have expanded to include other indices at global

* Corresponding author.
E-mail address: kdahlin@msu.edu (K.M. Dahlin).

https://doi.org/10.1016/j.jag.2018.02.017
Received 6 October 2017; Received in revised form 20 February 2018; Accepted 26 February 2018
Available online 10 March 2018
0303-2434/

scales. For example, Zhu et al., (2017) compared fifteen teleconnection patterns to the output from nine dynamic global vegetation models with standardized forcings. They found that the teleconnections were strongly connected to modelled gross primary productivity (GPP), with most areas strongly linked to ENSO, the Atlantic Meridional Mode, and the Pacific Decadal Oscillation. Gonsamo et al. (2016) compared the 30 year NDVI record (NDVI3 g; Pinzon and Tucker, 2014) to eight teleconnection indices. These authors also compared their set of teleconnection indices to net primary productivity from a coupled Earth system model and found that the model was unable to capture the spatial patterns observed in the data.

Instead of testing a large number of possibly cross-correlated teleconnection patterns (Quadrelli and Wallace, 2004), here we elected to document the impacts of two well-studied global teleconnections patterns—ENSO and NAO − and two infrequently considered climate modes − the Indian Ocean Dipole Mode (IODM) and the Atlantic Meridional Mode (AMM). We compare these four teleconnection patterns to land surface vegetation over a time span of 30 years, using the AVHRR-derived Leaf Area Index (LAI3 g) data set (Zhu et al., 2013). The temporal span of this product allows us to consider global connections between the land surface and the climate system that are not possible with shorter time series or locally focused analyses. These four teleconnection patterns represent spatially distinct climatological patterns from around the globe.

ENSO, perhaps the most well-known climatological pattern to ecologists and natural resource managers, is defined by changes in sea surface temperatures (SSTs) in the tropical Pacific, known as El Niño, which is linked to fluctuations in the distribution of atmospheric mass (called the Southern Oscillation; hence the term “El Niño/Southern Oscillation” or ENSO). These variations in the coupled ocean-atmosphere system set up “ripples” in the troposphere, which in turn affect global circulation patterns downstream. ENSO is associated with drought conditions in areas that are usually wet (i.e. Indonesia, southern Africa, India) and heavy rains in dry regions like the equatorial central Pacific, California, and the U.S. Gulf Coast (Rasmusson and Wallace, 1983). Here we describe ENSO using the Oceanic Niño Index (ONI) for December-January-February (DJF) which is a 3-month mean of sea surface temperature (SST) anomalies in the equatorial Pacific (Niño 3.4 region: 5°N–5°S, 120°–170°W (Huang et al., 2015)). Further increases in greenhouse gas concentrations are expected to lead to changes in the mean state of the Pacific Ocean and therefore possibly lead to more strong El Niño and La Niña years with fewer mild years (Cai et al., 2015).

The NAO is a measure of the difference in atmospheric conditions between the subtropical Atlantic and the Arctic (Stenseth et al., 2003). During its positive phase it has been associated with above average temperatures in the Eastern U.S. and northern Europe and below average temperatures in southern Europe and the Middle East and the reverse in the negative phase. Positive phases of the NAO are also associated with higher precipitation in northern Europe, lower precipitation in southern Europe. Similar to ENSO, a wide range of ecological impacts have been attributed to the NAO (de Beurs and Henebry, 2010, 2008; Vicente-Serrano and Trigo, 2011). Feedbacks between the NAO and future climate projections are complex, however, it is possible that a weakening of the NAO could lead to reduced losses of sea ice and fewer tropical storms (Delworth et al., 2016).

The AMM is a measure of SST anomalies in the tropical Atlantic Ocean where SSTs are warmer than usual in the tropical North Atlantic and cooler than usual in the tropical South Atlantic (Nobre and Shukla, 1996). This change in SSTs in turn impacts the location of the Intertropical Convergence Zone (ITCZ) and can change the timing and magnitude of precipitation events throughout the tropics, particularly in northeastern Brazil and the Sahel (Foltz et al., 2012). Because changes in the AMM influence wind patterns, strong AMM events are also associated with increased hurricane activity (Vimont and Kossin, 2007). Few studies have been done of the direct impacts of the AMM on the terrestrial biosphere, however, recent work has suggested that the AMM may play a role in tropical forest dynamics through a combination of hurricane and drought impacts (Chen et al., 2015).

The IODM (Saji et al., 1999) is a pattern of variability originating in the Indian Ocean, with cool SSTs near Sumatra linked to warm SSTs near East Africa. While somewhat correlated with ENSO (Saji and Yamagata, 2003), the impacts of the IODM appear to be much more focused on the countries surrounding the Indian Ocean − anomalously strong rainfall events in East Africa, central India, and Central/Eastern China are all much more closely tied to the IODM than to ENSO (Marchant et al., 2006; Pervez and Henebry, 2015). Importantly, future predictions for the IODM suggest that while its frequency is unlikely to change, the intensity of events will probably increase in coming decades under the influence of climate change (Cai et al., 2013).

Since these teleconnection patterns can often generate conflicting conditions for optimal plant growth (e.g., cooler temperatures and more rainfall), their expected impact on the biosphere is unclear. Each teleconnection is characterized by both a time series “index” of its amplitude through time, as well as a spatial map of its expression in various meteorological fields used to define it. Here we focus on the temporal indices of each pattern to isolate their influence on the terrestrial biosphere through time, across space, and within the annual cycle.

This paper addresses three questions related to the interactions between teleconnection patterns and the terrestrial biosphere: 1) What fraction of global interannual variation in LAI can be linked to two common and two less well studied teleconnection patterns? 2) How do the spatial patterns of impact vary among the different teleconnections? 3) How can we map these connections while taking account for temporal autocorrelation in the data in a simple and consistent manner?

2. Materials and methods

To assess linkages between the four teleconnection indices and local vegetation, we calculated correlations between each index averaged for December, January, and February (DJF) of a given year and LAI3 g minimum, mean, and maximum values for the subsequent three-month intervals (JFM, FMA, through DJ_2F_2 with J_2F_2 being from the following year). All analyses were performed at 0.25° resolution. We used a Monte Carlo approach to eliminate small patches of possibly spurious correlations, likely to be due to temporal autocorrelation. Finally, we aggregated the global correlation fields (36 per teleconnection pattern) to produce single maps of the strongest overall correlations and their seasonality.

Correlation Analysis. The central goal of this paper was to map the correlations between teleconnection pattern indices and variations in the land surface in a way that is permissive enough to capture small but significant relationships, but simple enough to be generalized and interpreted. All analyses were performed in R (RCoreTeam, 2015) using the raster (Hijmans and van Etten, 2013), rgdal (Bivand et al., 2013), and ncdf4 (Pierce, 2015) packages. All maps were made in ArcGIS 10.2.2. Fig. S1 shows a schematic of the analysis process.

In order to have a long enough time series to perform robust correlations, we used the AVHRR derived leaf area index data set (LAI3 g (Zhu et al., 2013)), which is a global data set of LAI for the complete years of 1982–2011 twice per month at twelfth-degree scale. To simplify data processing and to average over small scale changes in local vegetation, these data were rescaled (averaged) to quarter degree resolution. If a 0.25° grid cell had less than 60% coverage it was removed from further analysis, thus many coastal areas were excluded from analysis. Teleconnection pattern indices were obtained from the U.S. National Oceanic and Atmospheric Administration (NOAA, 2017, 2015a, 2015b, 2015c). To simplify comparisons, we selected the three month December-January-February period (‘DJF’; averaged) of each index to compare to subsequent months’ LAI values. DJF was selected for these indices as it is the 3-month period in the first half of the year with the highest interannual standard deviation in all four indices. Fig.

S2 shows the temporal patterns of these indices.

All of the indices were then normalized (mean = 0, s.d. = 1). Only the AMM had a significant trend ($p < 0.05$) so it was detrended (Fig. S2). This trend is likely due to the fact that the time period we considered (1982–2011) overlaps with first a negative phase in the Atlantic Multidecadal Oscillation (AMO) then a positive phase in the AMO. Patterns in the AMM are closely tied to the AMO (Vimont and Kossin, 2007). To test whether these indices were correlated with each other we constructed a correlation matrix (Fig. S3). While ENSO and the IODM are significantly correlated ($R^2 = 0.45$), we elected to use both of these indices in our analyses as there is evidence that they have substantially different impacts on weather patterns around the world (Saji et al., 1999; Saji and Yamagata, 2003).

To best capture the different potential lags between strong teleconnection timing and vegetation, we created maps of many different correlations then filtered the strongest ones to create our final aggregated maps. We first calculated point-wise correlations between each teleconnection index and the detrended where necessary, normalized (mean = 0, s.d. = 1) minimum, mean, and maximum LAI values for three-month moving windows for the following calendar year. We tested correlations between each index and minimum, mean, and maximum LAI values for JFM, FMA, MAM, etc, through DJ_2F_2 with J_2 and F_2 being from the following year. We then removed pixels with non-significant ($p < 0.05$) correlations from each of the correlation maps. This approach allowed us to isolate the strongest possible correlation throughout the year, instead of focusing on growing season values or annual averages. This also accounts for possible hemispherical differences, as a strong correlation between, for example, ENSO and maximum LAI in May in California would be represented equal to a strong correlation between ENSO and LAI in South Africa in December.

In order to address the issue of temporal autocorrelation without testing and correcting each model at each pixel, which would make the mapped results very difficult to interpret, we normalized and detrended the data as described previously then used a Monte Carlo-type approach. While any significant time series correlation could be the result of autocorrelation, here we argue that geographically large patches of significant correlations are unlikely to occur randomly. To test this assumption, we correlated each teleconnection index with 1000 stacks of 30 maps of randomly generated data with mean = 0 and s.d. = 1, as in the centered and scaled LAI over the 30-year time series, masked to match the continental outlines and no-data regions in the LAI3 g data (producing 4000 correlations maps total). We then identified individual patches using a 'Queen's case' approach (two grid cells are considered connected if they share a side or a corner), calculating the patch sizes within each map using the area function in the raster package in R. This function approximates area changes due to shifts in latitude by calculating the area of each grid cell as the height in km by the width at the center of the grid cell. We then selected the average maximum size of these random correlation patches to be the threshold below which patches of correlation would likely be spurious (overall average was 4790 km^2, which, for simplicity, we rounded up to 5000 km^2). There was no significant difference between the average maximum patch sizes for the four climate modes correlated with random values (ANOVA $p = 0.401$). We identified individual patches of correlation in the real data, also using the Queen's case, then calculated the area of each patch. We removed patches that were smaller than 5000 km^2 from each individual correlation map (e.g. ENSO DJF ~ AMJ max LAI) before stacking and aggregating the correlation maps.

The LAI3 g product is not a perfect representation of actual LAI, however, it is the only global LAI data set available that spans such a long time period. The two major sources of uncertainty in remote sensing of LAI are related to near infrared saturation at high LAI values (Gamon et al., 1995) and the myriad causes of seasonal variations (or their absence) in the tropics (Morton et al., 2014). We indirectly addressed these two issues by focusing on the variation, not the magnitude, of LAI around the world (all values were centered and normalized), by eliminating small patches of correlation, and by considering interannual variability, not intra-annual − e.g. correlations are calculated between a given teleconnection pattern and a value from the same 3 month period every year, so seasonal changes in sun angle should not impact these relationships.

To summarize these analyses, we selected the strongest significant correlations (maximum absolute value of Pearson's R) across the twelve time periods and min/mean/max values. We generated maps of the correlation values and identified the correlation time periods and min/mean/max (referred to below as 'identity maps'). The correlation value maps allow for visual interpretation of broad patterns, while the identity maps allow readers to see which areas correlate with which time period and value. While much longer lagged effects of teleconnection patterns are possible, here we elected to keep the time period relatively short (1 year) to avoid confusing the next year's pattern with the pattern in the current year. Finally, we summarized the area of positive and negative correlation by continent and by biome, using the biome boundaries defined by the World Wildlife Fund (Fig. S8) (Olson et al., 2001).

3. Results

Collectively, the four climate modes considered here affect nearly 70% (99.7 million km^2) of the world's land total area (correlation areas by continent in Table S1). These climate patterns influence processes in many of the most carbon-rich, food-insecure and biodiverse parts of the world (Fig. 1). The NAO has the most extensive reach, influencing 48% of the terrestrial land surface (70 million km^2), and ENSO exerts widespread influence, affecting 36% of the terrestrial land surface (52 million km^2). The AMM and IODM influence all vegetated continents, affecting 28% (41.5 million km^2) and 29% (43 million km^2) of land surface, respectively. As expected (Stenseth et al., 2003), ENSO has strong influences on western North America, the southern Amazon, and eastern and southern Africa (Indeje et al., 2000; Schonher and Nicholson, 1989), but also in Eastern Europe and the Siberian Plateau (Figs. 1 and 3B and S5). The NAO is felt most strongly in the Northern Hemisphere, but is correlated with LAI patterns around the world (Figs. 1 and 3D and S7). The AMM impacts the northern Amazon and Subequatorial Africa, but also the North American Great Plains and the Central Siberian Plateau (Figs. 1 and 3A and S4). The IODM has very strong correlations with LAI in Eastern and Southern Africa, but is also connected to LAI patterns in central Siberia and Southeast Asia (Figs. 1 and 3C and S6).

At the biome scale, none of these biosphere-atmosphere correlations show an exclusively positive or negative relationship (Fig. 2). Tropical and subtropical moist broadleaf forests and tropical grasslands, savannas, and shrub-lands show the most consistent patterns in terms of the sign of the relationship (Fig. 2A and G), with most of the area of these biomes having a positive correlation with the AMM and a negative correlation with the NAO (and to a lesser degree with ENSO). The other biome-level correlations are somewhat evenly split between positive and negative relationships. The distribution of impacts is also not evenly distributed among biomes, with some very small biomes, like tropical coniferous forests (Fig. 2C) and flooded grasslands (Fig. 2I), representing a small global land area that is almost uniformly linked to one or more teleconnection pattern.

The seasonality of the relationships between the teleconnection patterns and the biosphere reveal some large, spatially contiguous patterns but also more complexity in biosphere-atmosphere interactions within and among biomes (Fig. 3). The IODM and the NAO appear to have stronger relationships with LAI in the spring in the high latitudes of Asia, for example, while the NAO has a stronger influence in the fall in northern North America. The AMM has a broad positive relationship with LAI across the Amazon (Fig. 1A) but the seasonality of that relationship varies, with the northernmost part of South America most tightly coupled to the AMM around January, while the central Amazon

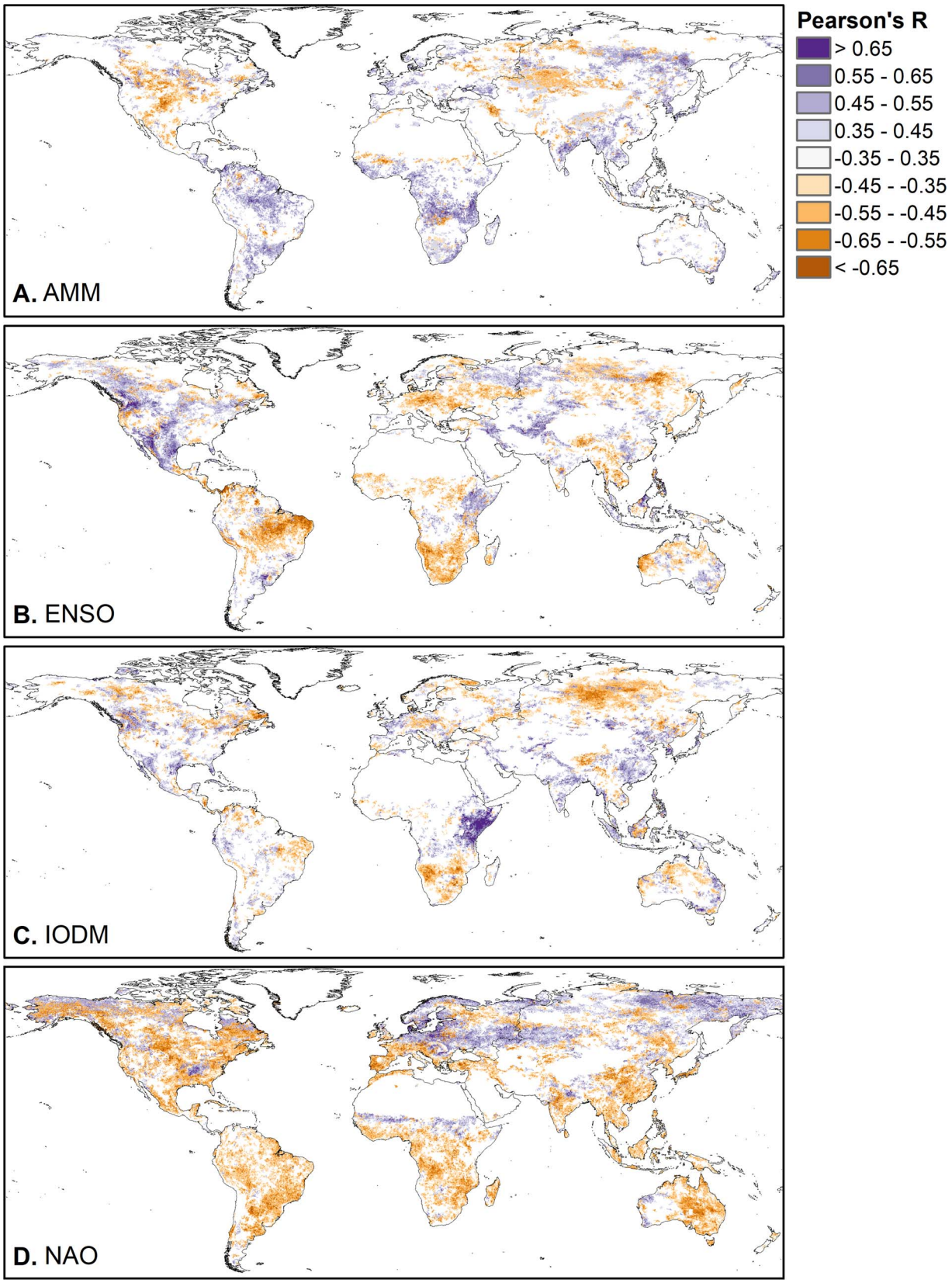

Fig. 1. Maximum teleconnection absolute correlations (Pearson's R). Each pixel represents the absolute maximum correlation between a teleconnection index and LAI, where the LAI value could be the minimum, mean, or maximum from any three-month period in the year. White land areas had either no vegetation data or no significant correlations.

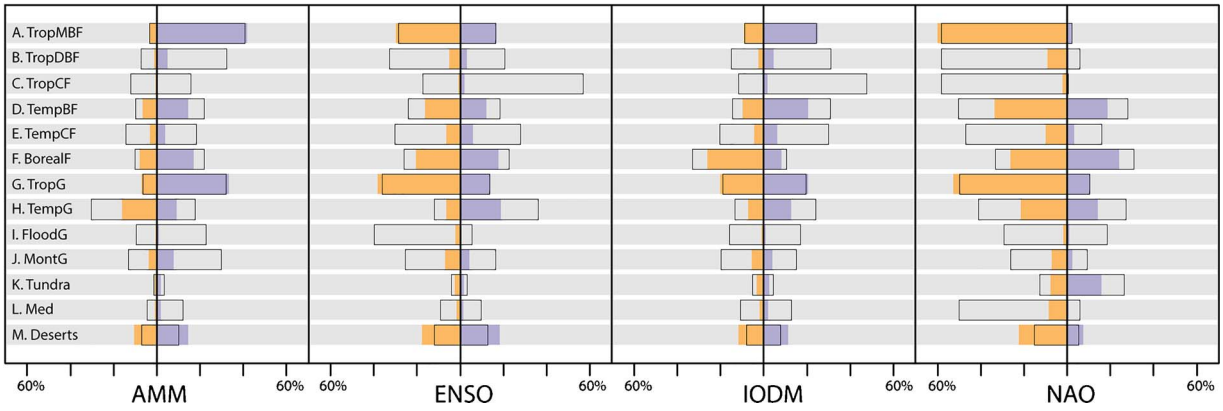

Fig. 2. Areas and fractions of correlation with teleconnections by biome. Blue bars show areas of positive correlation, orange bars show areas of negative correlation. The largest area of correlation is a negative correlation over 11.5 million km^2 for NAO with (A) TropMBF (abbreviations listed below). Colored area bars are scaled such that the 60% tick marks are equal to 11.5 million km^2. Percentages are shown with the open bars. The total area of TropMBF is 19.8 million km^2, so the NAO has a negative correlation with 58% of TropMBF. Biome x climate mode relationships with very small colored bars but large open bars (e.g. L. Med x NAO) have an overall small area but a large fraction of that area is impacted by the climate mode. When the colored bars extend beyond the open bars this means the area impacted is small relative to the size of the biome (e.g. M. Deserts). So, for example, a larger area of deserts have a negative relationship with the NAO than do Mediterranean systems, but a much larger fraction of Mediterranean systems are impacted by the NAO. A. TropMBF = Tropical and subtropical moist broadleaf forest; B. TropDBF = Tropical and subtropical dry broadleaf forest; C. TropCF = Tropical coniferous forest; D. TempBF = Temperate broadleaf and mixed forest; E. TempCF = Temperate Coniferous Forest; F. BorealF = Boreal Forests/Taiga; G. TropG = Tropical and subtropical grasslands, savannas, and shrublands; H. TempG = Temperate grasslands, savannas, and shrublands; I. FloodG = Flooded grasslands and savannas; J. MontG = Montane grasslands and shrublands; K. Tundra = Tundra; L. Med = Mediterranean forests, woodlands, and scrub; and M. Deserts = Deserts and xeric shrublands. Area and percent values listed in Table S2. (For interpretation of the references to colour in this figure legend, the reader is referred to the web version of this article.)

shows a stronger relationship in June/July (Fig. 3 and S4). In contrast, ENSO's influence dominates the southern Amazon but is most strongly coupled in July/August.

The largest contiguous area of correlation revealed in Fig. 3 is the connection between the IODM and northern East Africa (the red area in Fig. 3 includes southern Ethiopia, Somalia, Kenya, Uganda, and northern Tanzania). This area is generally characterized by having two rainy seasons per year: the long rains of March to June and the short rains of October to December. That the strongest correlation between the IODM and LAI is in January suggests that the IODM has a stronger influence over the short rains, as has been described in the atmospheric sciences literature (Ummenhofer et al., 2009).

4. Discussion

Climate teleconnection patterns influence the terrestrial biosphere in many different ways, depending on the location, vegetation types, land use history, and more. Assessing the relationships between climate teleconnections and LAI around the globe, using a simple but robust approach, has allowed us to identify areas that may be particularly vulnerable to changes in atmospheric and oceanic circulation patterns. Moreover, our analyses show that the influence of these teleconnection patterns is wider and more diverse than was previously understood.

Many studies have focused on the impacts of the NAO or ENSO on ecosystems, with tens of thousands of returns found for either on Google Scholar (i.e. a search for "El Niño Southern Oscillation" and ecology yielded > 23,000 results). Our study suggests that less well studied climate modes like the AMM and the IODM warrant more attention from ecologists and natural resource managers interested in the influence of climate on their field sites. For climate scientists, our study shows the importance of these large-scale phenomena on the biosphere; understanding how these teleconnection patterns may change in the future will be critical to understanding the carbon cycle in general, but also for food security, human health, and biodiversity conservation. For example, if the AMO shifts into a negative phase, how will this impact the AMM, and the ecosystems that are strongly connected to it, like those in southern Africa and the North American wheat belt?

Uncertainties in the sign and magnitude of terrestrial climate-carbon cycle feedbacks have preoccupied global ecologists, climate scientists, and Earth System Model (ESM) developers for decades (Friedlingstein et al., 2006; Shukla et al., 1990; Swann et al., 2012). Model-based studies have shown fine-scale and patchy responses by the terrestrial biosphere to relatively coarse changes in atmospheric forcings over longer time scales (Gonsamo et al., 2016; Swann et al., 2012); our analysis is based on observations, not ESM output, and therefore corroborates these complex results. Furthermore, we argue that generalizations of how terrestrial biomes or plant functional groups might respond to climate change are likely too coarse to capture the variety of ways that individual ecosystems respond to interannual variability in the climate in the short- or long-term.

Climate teleconnections patterns disrupt vegetation activity in many of the world's "biodiversity hotspots," defined as areas that are both biodiverse and threatened by humans (Myers et al., 2000; Pimm et al., 2014). While many of the threats to global biodiversity are clearly not directly due to interannual climate variability (e.g., poaching, habitat loss, and pest and pathogen spread (Dirzo et al., 2014; Sala et al., 2000; Yap et al., 2015)), our results identify Eastern and Southern Africa, Central America, the Brazilian Cerrado, and Southeast Asia (Figs. 1 and 3) as regions where climate could further threaten biodiversity. These maps also have the potential to help identify smaller areas of ecological importance. For example, a strong connection is identified between ENSO and the Guyanan savannas at the intersection of Brazil, Venezuela, and Guyana. While the high biodiversity of this region is known (de Carvalho and Mustin, 2017), other 'teleconnection hotspots' could signal high concentrations of biodiversity as well. Our analysis suggests that parts of the world with high biodiversity, large human populations, and strong biosphere-atmosphere connections are some of the most likely to be at risk for biodiversity loss, although the details of how habitat heterogeneity and climate variability influence biodiversity are only beginning to be addressed at regional to global scales (Tuanmu and Jetz, 2015). Shifts in the climate teleconnection patterns in these regions would likely have cascading impacts both directly on biodiversity and indirectly through increased human pressures. For example, fire is an important part of African ecosystems (Archibald, 2016); spatial or temporal shifts in rainfall patterns could influence natural and anthropogenic fire return intervals that would in turn impact tree fractional cover and animal habitat.

Many of the regions highlighted in our analysis are major agricultural regions, including North America and Central Asia (impacted by AMM and NAO), subequatorial Africa (impacted by AMM), Central

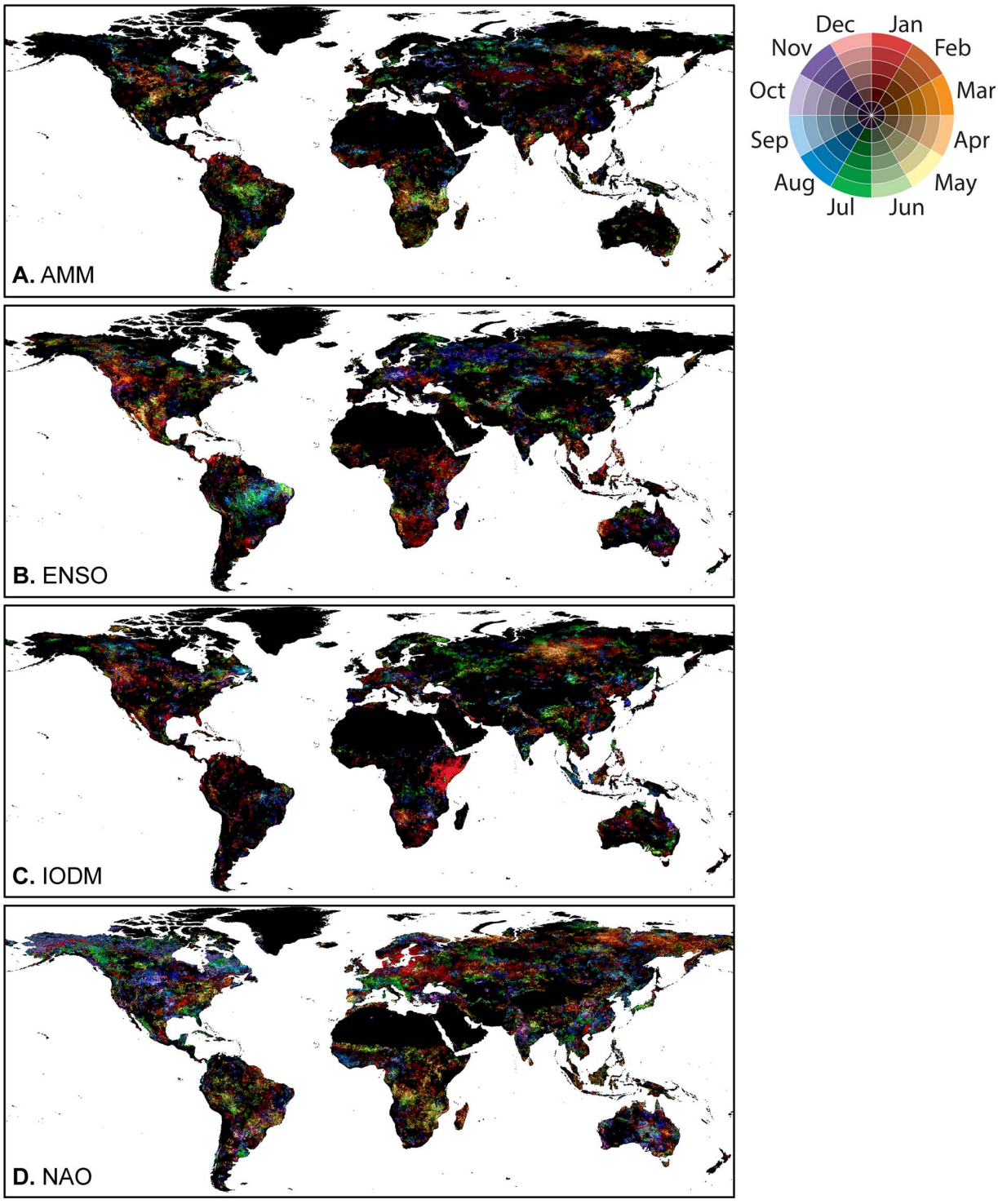

Fig. 3. Maximum teleconnection month x LAI coefficients of determination (R^2). Mapped across all months' minimum, mean, or maximum LAI values, so pixels with correlations are the same as in Fig. 1. Brighter colors are stronger R^2s, darker are weaker or zero. Each month has six possible color values, with the brightest being R^2s $>=0.4$, then, in descending order, 0.4 to 0.325 to 0.25 to 0.175 to 0.1 to 0.

America and Eastern Europe (impacted by ENSO), East Africa (impacted by IODM), and the Mediterranean, India, Australia, eastern South America, and China (impacted by NAO). Jointly, these areas comprise the majority of rain-fed agricultural lands and pastures (Ramankutty et al., 2008). In the northern latitudes our results corroborate patterns found by Wright et al. (2014) that there is a positive relationship between the NAO and NDVI in the Eurasian Wheat Belt., while in Africa our results corroborate the complex spatial patterns found by Brown et al. (2010). In recent decades many of these regions have undergone food shortages due to weather anomalies and human health has suffered as a consequence (Battisti and Naylor, 2009). For example, the lowest values for the DJF IODM since 1982 were in 1997, 1999, 2011, and 2017 (−0.82, −0.81, −0.57, and −0.63, respectively) (NOAA, 2017). These years correspond closely with several of the major famines in East Africa, including those in 1998 in Sudan (Deng, 2002), 1998–2000 in Ethiopia (White, 2005), 2011–2012 in Somalia (Maxwell and Fitzpatrick, 2012), and 2017 in South Sudan (FEWS, 2017). The influence of technological advances on food security

makes it difficult to predict how future changes in teleconnection patterns will impact food security. However, given current technologies and resources a significant shift in the magnitude or frequency of any of these four climate teleconnection patterns would have dramatic impacts on our global food system.

5. Conclusion

Increasing focus is being placed on understanding eco-climate teleconnections (Swann et al., 2012) − that is, how biosphere-atmosphere feedbacks will impact not just local conditions, but other regions around the world. Correctly representing climate teleconnection patterns has been a key focus of atmospheric science and a way of assessing general circulation model performance (Bellenger et al., 2014), while representing vegetation phenology has been a central focus in the land modelling community (Caldararu et al., 2014; Dahlin et al., 2015; Richardson et al., 2012; Stockli et al., 2011). The next challenge will be to understand and predict how changes to one or more of these components of the Earth system might affect the current levels of interannual variability that have supported diverse biological and economic systems for centuries. Changes to the timing and magnitude of high frequency events like these teleconnection patterns, superimposed on long-term changes in average conditions due to climate change, are likely to drive abrupt shifts in agro-ecological systems with far reaching impacts on humans and the environment.

Data availability

Full resolution GeoTIFFs of all maps are available via FigShare (https://doi.org/10.6084/m9.figshare.5948404). The LAI3 g product was obtained from Dr. Ranga Myneni's group (http://sites.bu.edu/cliveg/files/2014/08/gimms_list.txt), and climate pattern data are available online from original sources as cited.

Author contributions

KMD and TRA designed the research. KMD conducted the research. Both authors contributed to the writing of the manuscript.

Acknowledgements

This work was supported in part by the National Center for Atmospheric Research (NCAR) Advanced Study Program. We would like to acknowledge high-performance computing support from Yellowstone (ark:/85065/d7wd3xhc) provided by NCAR's Computational and Information Systems Laboratory. NCAR is sponsored by the National Science Foundation.

Appendix A. Supplementary data

Supplementary data associated with this article can be found, in the online version, at https://doi.org/10.1016/j.jag.2018.02.017.

References

Archibald, S., 2016. Managing the human component of fire regimes: lessons from Africa. Philos. Trans. R. Soc. B Biol. Sci. 371, 20150346. http://dx.doi.org/10.1098/rstb.2015.0346.

Barnston, A.G., Livezey, R.E., 1987. Classification, seasonality and persistence of low-frequency atmospheric circulation patterns. Mon. Weather Rev. 115, 1083–1126. http://dx.doi.org/10.1175/1520-0493(1987)115<1083:CSAPOL>2.0.CO;2.

Battisti, D., Naylor, R.L., 2009. Historical warnings of future food insecurity with unprecedented seasonal heat. Science (80-.) 323, 240–244.

Bellenger, H., Guilyardi, E., Leloup, J., Lengaigne, M., Vialard, J., 2014. ENSO representation in climate models: from CMIP3 to CMIP5. Clim. Dyn. 42, 1999–2018. http://dx.doi.org/10.1007/s00382-013-1783-z.

Bivand, R., Keitt, T., Rowlingson, B., 2013. Rgdal: Bindings for the Geospatial Data Abstraction Library.

Bonan, G.B., 2008. Ecological Climatology. Cambridge University Press, Cambridge, UK.

Brown, M.E., de Beurs, K., Vrieling, A., 2010. The response of African land surface phenology to large scale climate oscillations. Remote Sens. Environ. 114, 2286–2296. http://dx.doi.org/10.1016/j.rse.2010.05.005.

Cai, W., Zheng, X.-T., Weller, E., Collins, M., Cowan, T., Lengaigne, M., Yu, W., Yamagata, T., 2013. Projected response of the Indian Ocean Dipole to greenhouse warming. Nat. Geosci. 6, 999–1007. http://dx.doi.org/10.1038/ngeo2009.

Cai, W., Santoso, A., Wang, G., Yeh, S.-W., An, S.-I., Cobb, K.M., Collins, M., Guilyardi, E., Jin, F.-F., Kug, J.-S., Lengaigne, M., McPhaden, M.J., Takahashi, K., Timmermann, A., Vecchi, G., Watanabe, M., Wu, L., 2015. ENSO and greenhouse warming. Nat. Clim. Chang. 5, 849–859. http://dx.doi.org/10.1038/nclimate2743.

Caldararu, S., Purves, D.W., Palmer, P.I., 2014. Phenology as a strategy for carbon optimality: a global model. Biogeosciences 11, 763–778. http://dx.doi.org/10.5194/bg-11-763-2014.

Charrette, N.A., Cleary, D.F., Mooers, A.Ø., 2006. Range-restricted, specialist Bornean butterflies are less likely to recover from ENSO-induced disturbance. Ecology 87, 2330–2337. http://dx.doi.org/10.1890/0012-9658(2006)87[2330:RSBBAL]2.0.CO;2.

Chen, Y., Randerson, J.T., Morton, D.C., 2015. Tropical North Atlantic ocean-atmosphere interactions synchronize forest carbon losses from hurricanes and Amazon fires. Geophys. Res. Abstr. 6462–6470. http://dx.doi.org/10.1002/2015GL064505. (Received).

Dahlin, K.M., Fisher, R.A., Lawrence, P.J., 2015. Environmental drivers of drought deciduous phenology in the Community Land Model. Biogeosciences 12, 5061–5074. http://dx.doi.org/10.5194/bg-12-5061-2015.

Delworth, T.L., Zeng, F., Vecchi, G.A., Yang, X., Zhang, L., Zhang, R., 2016. The North Atlantic Oscillation as a driver of rapid climate change in the Northern Hemisphere. Nat. Geosci. 9, 509–512. http://dx.doi.org/10.1038/ngeo2738.

Deng, L.B., 2002. The Sudan famine of 1998. IDS Bull. 33, 28–38.

Dirzo, R., Young, H.S., Galetti, M., Ceballos, G., Isaac, N.J.B., Collen, B., 2014. Defaunation in the anthropocene. Science (80-.). 345, 401–406. http://dx.doi.org/10.1126/science.1251817.

FEWS, 2017. Famine (IPC Phase 5) possible in South Sudan during 2017 [WWW Document]. Famine Early Warn. Syst. Netw. URL http://www.fews.net/east-africa/south-sudan/alert/january-18-2017 (Accessed 3.21.17).

Foltz, G.R., McPhaden, M.J., Lumpkin, R., 2012. A strong atlantic meridional mode event in 2009: the role of mixed: layer dynamics. J. Clim. 25, 363–380. http://dx.doi.org/10.1175/JCLI-D-11-00150.1.

Friedlingstein, P., Cox, P., Betts, R., Bopp, L., von Bloh, W., Brovkin, V., Cadule, P., Doney, S., Eby, M., Fung, I., Bala, G., John, J., Jones, C., Joos, F., Kato, T., Kawamiya, M., Knorr, W., Lindsay, K., Matthews, H.D., Raddatz, T., Rayner, P., Reick, C., Roeckner, E., Schnitzler, K.-G., Schnur, R., Strassmann, K., Weaver, A.J., Yoshikawa, C., Zeng, N., 2006. Climate?Carbon cycle feedback analysis: results from the C4MIP model intercomparison. J. Clim. 19, 3337–3353. http://dx.doi.org/10.1175/JCLI3800.1.

Gamon, J.A., Field, C.B., Goulden, M.L., Griffin, K.L., Hartley, E., Joel, G., Peñuelas, J., Valentini, R., 1995. Relationships between NDVI, canopy structure, and photosynthesis in three Californian vegetation types. Ecol. Appl. 5, 28–41.

Gonsamo, A., Chen, J.M., Lombardozzi, D., 2016. Global vegetation productivity response to climatic oscillations during the satellite era. Glob. Chang. Biol. 22, 3414–3426. http://dx.doi.org/10.1111/gcb.13258.

Hijmans, R.J., van Etten, J., 2013. Raster: Geographical Data Analysis and Modeling.

Huang, B., Banzon, V.F., Freeman, E., Lawrimore, J., Liu, W., Peterson, T.C., Smith, T.M., Thorne, P.W., Woodruff, S.D., Zhang, H.-M., 2015. Extended reconstructed sea surface temperature version 4 (ERSST. v4). Part I: upgrades and intercomparisons. J. Clim . 4, 911–930. http://dx.doi.org/10.1175/JCLI-D-14-00006.1.

Indeje, M., Semazzi, F.H.M., Ogallo, L.J., 2000. ENSO signals in East African rainfall seasons. Int. J. Climatol. 46, 19–46.

Li, J., Fan, K., Xu, Z., 2016. Links between the late wintertime North Atlantic Oscillation and springtime vegetation growth over Eurasia. Clim. Dyn. 46, 987–1000. http://dx.doi.org/10.1007/s00382-015-2627-9.

Marchant, R., Mumbi, C., Behera, S., Yamagata, T., 2006. Review paper the Indian Ocean dipole − the unsung driver of climatic variability in east africa. Afr. J. Ecol. 45, 4–16. http://dx.doi.org/10.1111/j.1365-2028.2006.00707.x.

Maxwell, D., Fitzpatrick, M., 2012. The 2011 Somalia famine: context, causes, and complications. Glob. Food Sec. 1, 5–12. http://dx.doi.org/10.1016/j.gfs.2012.07.002.

Maza-Villalobos, S., Poorter, L., Martínez-Ramos, M., 2013. Effects of ENSO and temporal rainfall variation on the dynamics of successional communities in old-field succession of a tropical dry forest. PLoS One 8. http://dx.doi.org/10.1371/journal.pone.0082040.

McPhaden, M.J., Zebiak, S.E., Glantz, M.H., 2006. ENSO as an integrating concept in earth science. Science (80-.) 314, 1740–1745. http://dx.doi.org/10.1126/science.1132588.

Morton, D.C., Nagol, J., Carabajal, C.C., Rosette, J., Palace, M., Cook, B.D., Vermote, E.F., Harding, D.J., North, P.R.J., 2014. Amazon forests maintain consistent canopy structure and greenness during the dry season. Nature 506, 221–224. http://dx.doi.org/10.1038/nature13006.

Myers, N., Mittermeier, R.A., Mittermeier, C.G., da Fonseca, G.A., Kent, J., 2000. Biodiversity hotspots for conservation priorities. Nature 403, 853–858. http://dx.doi.org/10.1038/35002501.

NOAA, 2015. El Nino-Southern Oscillation ONI 3.4 [WWW Document]. Natl. Ocean. Atmos. Adm. URL http://www.cpc.ncep.noaa.gov/products/analysis_monitoring/ensostuff/ensoyears.shtml (Accessed 6.2.15).

NOAA, 2015. Northern Hemisphere Teleconnection Patterns: Historical Archive of all Indices [WWW Document]. Natl. Ocean. Atmos. Adm. URL ftp://ftp.cpc.ncep.noaa.gov/wd52dg/data/indices/tele_index.nh (Accessed 3.23.15).

NOAA, 2015. Monthly Climate Timeseries: Atlantic Meridional Mode SST Index [WWW Document]. Natl. Ocean. Atmos. Adm. URL https://www.esrl.noaa.gov/psd/data/timeseries/monthly/AMM/ammsst.data (Accessed 11.11.15).
NOAA, 2017. Indian Ocean Dipole Mode Index [WWW Document]. Natl. Ocean. Atmos. Adm. URL http://stateoftheocean.osmc.noaa.gov/sur/ind/dmi.php (Accessed 3. 20.17).
Nobre, P., Shukla, J., 1996. Variations of sea surface temperature wind stress, and rainfall over the tropical Atlantic and South America. J. Clim. 9, 2464–2479. http://dx.doi.org/10.1175/1520-0442(1996)009<2464:VOSSTW>2.0.CO;2.
Ogutu, J.O., Owen-Smith, N., 2003. ENSO, rainfall and temperature influences on extreme population declines among African savanna ungulates. Ecol. Lett. 6, 412–419. http://dx.doi.org/10.1046/j.1461-0248.2003.00447.x.
Olson, D.M., Dinerstein, E., Wikramanayake, E.D., Burgess, N.D., Powell, G.V.N., Underwood, E.C., D'amico, J. a., Itoua, I., Strand, H.E., Morrison, J.C., Loucks, C.J., Allnutt, T.F., Ricketts, T.H., Kura, Y., Lamoreux, J.F., Wettengel, W.W., Hedao, P., Kassem, K.R., 2001. Terrestrial ecoregions of the world: a new map of life on earth. Bioscience 51, 933. http://dx.doi.org/10.1641/0006-3568(2001)051[0933:TEOTWA]2.0.CO;2.
Pervez, M.S., Henebry, G.M., 2015. Spatial and seasonal responses of precipitation in the Ganges and Brahmaputra river basins to ENSO and Indian Ocean dipole modes: implications for flooding and drought. Nat. Hazards Earth Syst. Sci. 15, 147–162. http://dx.doi.org/10.5194/nhess-15-147-2015.
Phillips, A.S., Deser, C., Fasullo, J., 2014. Evaluating modes of variability in climate models. Eos (Washington. DC). 95, 453–455. http://dx.doi.org/10.1038/nature1253.
Pierce, D., 2015. Interface to Unidata netCDF (version 4 or earlier) format data files [WWW Document]. R Packag. URL https://cran.r-project.org/web/packages/ncdf4/index.html (Accessed 5.1.16).
Pimm, S.L., Jenkins, C.N., Abell, R., Brooks, T.M., Gittleman, J.L., Joppa, L.N., Raven, P.H., Roberts, C.M., Sexton, J.O., 2014. The biodiversity of species and their rates of extinction, distribution, and protection. Science (80-.). 344, 1246752. http://dx.doi.org/10.1126/science.1246752.
Pinzon, J.E., Tucker, C.J., 2014. A non-stationary 1981–2012 AVHRR NDVI3 g time series. Remote Sens. 6, 6929–6960. http://dx.doi.org/10.3390/rs6086929.
Quadrelli, R., Wallace, J.M., 2004. A simplified linear framework for interpreting patterns of Northern Hemisphere wintertime climate variability. J. Clim. 17, 3728–3744. http://dx.doi.org/10.1175/1520-0442(2004)017<3728:ASLFFI>2.0.CO;2.
RCoreTeam, 2015. R: A Language and Environment for Statistical Computing.
Ramankutty, N., Evan, A.T., Monfreda, C., Foley, J.A., 2008. Farming the planet: 1. Geographic distribution of global agricultural lands in the year 2000. Glob. Biogeochem. Cycles 22, 1–19. http://dx.doi.org/10.1029/2007GB002952.
Rasmusson, E.M., Wallace, J.M., 1983. Meterological aspects of the El Niño/Southern oscillation. Science (80-.) 222, 1195–1202.
Richardson, A.D., Anderson, R.S., Arain, M.A., Barr, A.G., Bohrer, G., Chen, G., Chen, J.M., Ciais, P., Davis, K.J., Desai, A.R., Dietze, M.C., Dragoni, D., Garrity, S.R., Gough, C.M., Grant, R., Hollinger, D.Y., Margolis, H. a., McCaughey, H., Migliavacca, M., Monson, R.K., Munger, J.W., Poulter, B., Raczka, B.M., Ricciuto, D.M., Sahoo, A.K., Schaefer, K., Tian, H., Vargas, R., Verbeeck, H., Xiao, J., Xue, Y., 2012. Terrestrial biosphere models need better representation of vegetation phenology: results from the North American Carbon Program Site Synthesis. Glob. Chang. Biol. 18, 566–584. http://dx.doi.org/10.1111/j.1365-2486.2011.02562.x.
Saji, N.H., Yamagata, T., 2003. Possible impacts of Indian Ocean Dipole mode events on global climate. Clim. Res. 25, 151–169. http://dx.doi.org/10.3354/cr025151.
Saji, N.H., Goswami, B.N., Vinayachandran, P.N., Yamagata, T., 1999. A dipole mode in the tropical Indian Ocean. Nature 401, 360–363. http://dx.doi.org/10.1038/43854.
Sala, O.E., Chapin III, F.S., Armesto, J., Berlow, E., Bloomfield, J., Dirzo, R., Huber-Sanwald, E., Huenneke, L., Jackson, R.B., Kinzig, A.P., Leemans, R., Lodge, D., Mooney, H.A., Oesterheld, M., Poff, N., Sykes, M., Walker, B., Walker, M., Wall, D., 2000. Global biodiversity scenarios for the year 2100. Science (80-) 287, 1770–1774. http://dx.doi.org/10.1126/science.287.5459.1770.
Schonher, T., Nicholson, S.E., 1989. The relationship between California rainfall and ENSO events. J. Clim. 2, 1258–1269. http://dx.doi.org/10.1175/1520-0442(1989)002<1258:TRBCRA>2.0.CO;2.
Shukla, J., Nombre, C., Sellers, P., 1990. Amazon deforestation and climate change. Science (80-.). 247, 1322–1325.
Stenseth, N.C., Ottersen, G., Hurrell, J.W., Mysterud, A., Lima, M., Chan, K.-S., Yoccoz, N.G., Adlandsvik, B., 2003. Studying climate effects on ecology through the use of climate indices: the North Atlantic Oscillation, El Niño Southern Oscillation and beyond. Proc. Biol. Sci. 270, 2087–2096. http://dx.doi.org/10.1098/rspb.2003.2415.
Stockli, R., Rutishauser, T., Baker, I., Liniger, M. a., Denning, a. S., 2011. A global reanalysis of vegetation phenology. J. Geophys. Res. Biogeosci. 116, 1–19. http://dx.doi.org/10.1029/2010JG001545.
Swann, A.L.S., Fung, I.Y., Chiang, J.C.H., 2012. Mid-latitude afforestation shifts general circulation and tropical precipitation. Proc. Natl. Acad. Sci. 109, 712–716. http://dx.doi.org/10.1073/pnas.1116706108.
Tuanmu, M.N., Jetz, W., 2015. A global, remote sensing-based characterization of terrestrial habitat heterogeneity for biodiversity and ecosystem modelling. Glob. Ecol. Biogeogr. 24, 1329–1339. http://dx.doi.org/10.1111/geb.12365.
Ummenhofer, C.C., Sen Gupta, A., England, M.H., Reason, C.J.C., 2009. Contributions of Indian Ocean sea surface temperatures to enhanced East African rainfall. J. Clim . 22, 993–1013. http://dx.doi.org/10.1175/2008JCLI2493.1.
Hydrological, Socioeconomic and Ecological Impacts of the North Atlantic Oscillation in the Mediterranean Region. In: Vicente-Serrano, S.M., Trigo, R.M. (Eds.), Springer Science + Business Media, New York, NY. http://dx.doi.org/10.1007/978-94-007-1372-7.
Vimont, D.J., Kossin, J.P., 2007. The Atlantic meridional mode and hurricane activity. Geophys. Res. Lett. 34, 1–5. http://dx.doi.org/10.1029/2007GL029683.
White, P., 2005. War and food security in Eritrea and Ethiopia, 1998–2000. Disasters 29, 92–113. http://dx.doi.org/10.1111/j.0361-3666.2005.00286.x.
Wright, C.K., de Beurs, K.M., Henebry, G.M., 2014. Land surface anomalies preceding the 2010 Russian heat wave and a link to the North Atlantic oscillation. Environ. Res. Lett. 9. http://dx.doi.org/10.1088/1748-9326/9/12/124015.
Yap, T.A., Koo, M.S., Ambrose, R.F., Wake, D.B., Vredenburg, V.T., 2015. Averting a North American biodiversity crisis. Science (80-.) 349, 481–482. http://dx.doi.org/10.1126/science.aab1052.
Zhu, Z., Bi, J., Pan, Y., Ganguly, S., Anav, A., Xu, L., Samanta, A., Piao, S., Nemani, R., Myneni, R., 2013. Global Data Sets of Vegetation Leaf Area Index (LAI)3 g and Fraction of Photosynthetically Active Radiation (FPAR)3 g Derived from Global Inventory Modeling and Mapping Studies (GIMMS) Normalized Difference Vegetation Index (NDVI3 g) for the Period 1981–2. Remote Sens. 5, 927–948. http://dx.doi.org/10.3390/rs5020927.
Zhu, Z., Piao, S., Xu, Y., Bastos, A., Ciais, P., Peng, S., 2017. The effects of teleconnections on carbon fluxes of global terrestrial ecosystems. Geophys. Res. Lett. 44, 3209–3218. http://dx.doi.org/10.1002/2016GL071743.
de Beurs, K.M., Henebry, G.M., 2008. Northern annular mode effects on the land surface phenologies of northern Eurasia. J. Clim. 21, 4257–4279. http://dx.doi.org/10.1175/2008JCLI2074.1.
de Beurs, K.M., Henebry, G.M., 2010. A land surface phenology assessment of the northern polar regions using MODIS reflectance time series. Can. J. Remote Sens. 36, S87–S110. http://dx.doi.org/10.5589/m10-021.
de Carvalho, W.D., Mustin, K., 2017. The highly threatened and little known Amazonian savannahs. Nat. Ecol. Evol. 1, 100. http://dx.doi.org/10.1038/s41559-017-0100.